BOLETIN DE LA SOCIEDAD ESPAÑOLA DE
Cerámica y Vidrio
www.elsevier.es/bsecv

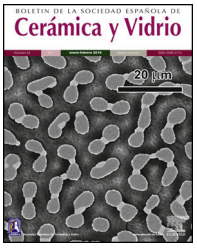

Original

Developing ABO_3 perovskites synthesized by the Pechini method for their potential application as cathode material in solid oxide fuel cells: Structural and electrical properties

Miguel Antonio Domínguez-Crespo[a,*], *Aidé Minerva Torres-Huerta*[a,*], *Silvia Beatriz Brachetti-Sibaja*[b], *Adela Eugenia Rodríguez-Salazar*[c], *Francisco Gutiérrez-Galicia*[a], *Esther Ramírez-Meneses*[d], *Ángela Iveth Licona-Aguilar*[b,e]

[a] *Instituto Politécnico Nacional, UPIIH, km 1+500, San Agustín Tlaxcala, Hgo, Mexico*
[b] *Tecnológico Nacional de México-IT de Ciudad Madero, D.E.P.I., Mexico*
[c] *Instituto Politécnico Nacional, CICATA Querétaro, Santiago de Querétaro, Querétaro, Mexico*
[d] *Departamento de Ingeniería Química, Industrial y de Alimentos, Universidad Iberoamericana, Ciudad de México, Mexico*
[e] *Tecnológico Nacional de México-IT de Celaya, Celaya, Guanajuato, Mexico*

ARTICLE INFO

Article history:
Received 5 April 2023
Accepted 21 September 2023
Available online 6 October 2023

Keywords:
$La_{0.7-x}Pr_xCa_{0.3}MnO_3$ (LPCM) perovskites
Pechini method
Rietveld analysis
Electrical measurements
SOFCs

ABSTRACT

In this research, the effect of La substitution by Pr cation in the A-site of ABO_3 perovskites was carried out using the Pechini method for use in solid state fuel cells (SOFCs). The atomic compositions of Pr varied from $x = 0.35, 0.49, 0.53, 0.56, 0.63$ and 0.7 in the $La_{0.7-x}Pr_xCa_{0.3}MnO_3$ (LPCM) perovskites. The XRD patterns indicated that all the perovskites crystallized in the orthorhombic system with *Pnma* space group, but only in atomic compositions of 0.53 and 0.70 is possible to obtain pure phases; whereas the other compositions present narrow peaks of La and Pr oxides that are reduced with the amount of the cationic substitution. The Rietveld methodology and its analysis by the Goldsmith tolerance factor indicated that the stability of the samples was achieved through Jahn-Teller distortion in the *b*-axis. The Mn^{3+}/Mn^{4+} atomic ratios determined by XPS measurements suggested that the substitution of La ions by Pr promotes the hole doped system instead of electron system. The electrical conductivity showed that the synthesized perovskites are mixed ionic and electronic conductors which positively influence their application in SOFCs. In particular, the $La_{0.17}Pr_{0.53}Ca0_{.3}MnO_3$ may be a good cathode candidate for these devices.

* *Corresponding authors.*
E-mail addresses: mdominguezc@ipn.mx (M.A. Domínguez-Crespo), atorresh@ipn.mx (A.M. Torres-Huerta).
https://doi.org/10.1016/j.bsecv.2023.09.001

Desarrollo de perovskitas ABO_3 sintetizadas por el método de Pechini para su potencial aplicación como material catódico en celdas de combustible de óxido sólido: propiedades estructurales y eléctricas

Palabras clave:
Perovkitas $La_{0.7-x}Pr_xCa_{0.3}MnO_3$ (LPCM)
Método Pechini
Análisis Rietveld
Mediciones eléctricas
SOFC

RESUMEN

En esta investigación, el efecto de la sustitución del catión Pr por el La en el sito de A de las perovskitas ABO_3 se llevó a cabo utilizando el método de Pechini para uso en celdas de combustible de estado sólido (SOFC). La composición atómica de Pr fue variada de $x = 0.35$, 0.49, 0.53, 0.56, 0.63 y 0.7 en las perovkitas $La_{0.7-x}Pr_xCa_{0.3}MnO_3$ (LPCM). Los patrones de DRX indicaron que todas las perovskitas cristalizaron en el sistema ortorrómbico con grupo espacial *Pnma*, pero únicamente de las composiciones atómicas de 0.53 y 0.70 es posible obtener fases puras; mientras que, otras composiciones presentan picos estrechos de óxidos de La y Pr que se reducen con la cantidad de sustitución catiónica. La metodología de Rietveld y el análisis realizado mediante el factor de tolerancia Goldsmith indicó que la estabilidad de las muestras fue lograda a través de la distorsión de Jahn-Teller en el eje-b. Los radios atómicos Mn^{3+}/Mn^{4+} indican que la sustitución de La por iones Pr promueve el sistema dopado a través de huecos. La conductividad eléctrica demostró que las perovskitas sintetizadas son conductores mixtos iónicos y electrónicos que influyen positivamente en la aplicación en SOFC. Particularmente, $La_{0.17}Pr_{0.53}Ca0_{.3}MnO_3$ es un buen cátodo para este tipo de dispositivos.

Introduction

Solid oxide fuel cells (SOFCs) are electrochemical energy conversion devices that directly convert chemical energy into electricity with high-energy conversion efficiency [1]. SOFCs are considered as low environmental impact devices with flexible fuel feeding, low carbon emissions and noise during the working process [2,3]. Typically, fuel cells require ceramic materials (cathode–electrolyte–anode) that present stability during the oxidation–reduction process (chemical, thermal and mechanical), adequate compatibility with electrolyte, hermeticity, porous structure for the adequate transport of gases to the cell active sites transportation to reaction sites and high electrical conductivity [4]. Unfortunately, the used materials still have significant drawbacks, such as high operating temperatures (800–1000 °C), long time required to heat and cool devices during operating cycles, degradation of components, thermal stress, and diffusion between components [5,6]. To overcome these disadvantages, different perovskite materials have been proposed to reduce the operating temperature between 600 and 800 °C, but also they reduce the catalytic activity and increase the applied bias on the cathode side, where cell performance plays a key role [5,7–9]. Stoichiometric and non-stoichiometric ABX_3 perovskites have been widely reported as cathode materials for IT-SOFCs [10–13]. In site A, La, Sr, Ca, Pb, and Pr have been explored, while in B-site cations of Ti, Mn, Ni, Fe, Co and Zr have been reported. The X-site is commonly occupied by oxygen with two types of sites, one with coordination six and others with coordination eight or twelve [14–16]. Among these perovskites, manganites with the general formula of $Ln_{1-x}M_xMnO_3$ (Ln = trivalent rare earth ions, alkaline rare earth element M = 3d transition) have been studied with a significant impact on the performance of SOFCs, which can be modulate depending on the ratio of Mn valences (Mn^{3+}/Mn^{4+}). This proportion has a direct influence on the performance of electrical and magnetic properties [17,18]. For example, lanthanum strontium manganite ($La_{1-x}Sr_xMnO_3$, LSM)-based perovskites showed high electrical conductivities due to distortions in their structures; that is, they are sensitive to the stoichiometry of the perovskite, relating the MnO_6 structure connectivity and the Jahn-Teller effect which in turn conditions its electron holes [19–21]. Therefore, perovskite-type manganites are considered the most versatile materials because they show high magnetoresistance, multiferroicity and have reasonable performance both as anode or cathode in IT-SOFCs using different fuels [21–27]. Although it occurs more severely at high temperatures (>750 °C) and high cell polarization, even at intermediate temperatures, loss of stability in reducing atmospheres has been observed on the cathodic side of IT-SOFCs devices. This instability causes diffusion and degradation in the cathode–electrolyte interface, with the consequent formation of insulating phases such as $La_2Zr_2O_7$ or $SrZrO_3$, negatively affecting ion conductivity [28]. The total or partial replacement of Sr in the A-site by other lanthanide elements such as Ce, Pr, Nd, Sm, and Gd or with Ca, Co, Cu, and Cr can contribute to the reduction of these disadvantages. For example, a reduction in the mismatch of the thermal expansion coefficient at the electrode–electrolyte interface, a reduction in the cell polarization, and an improvement in overall electro-catalytic activity have been reported [29–32]. Recently, it has been determined that the electrical and catalytic properties of lanthanum manganite perovskites depend to a large extent on the structure and morphology, but it is necessary to obtain pure phases during the synthesis [33,34]. In this way, Rietveld's refinement has been one of the

most useful techniques to quantitatively identify the phases and structural changes of this type of material [11,35–37]. Ongoing with the proposal of new materials for energy production that help to reduce cathodic polarization resistance and the operating temperatures, in this study, the analysis of different synthesis parameters was carried out to produce pure $La_{0.7-x}Pr_xCa_{0.3}MnO_3$ perovskites by lanthanum substitution ($x = 0.35$, 0.49, 0.53, 0.56, 0.63, and 0.7) through the Pechini sol–gel method. Rietveld refinement was carried out to evaluate the conditions under which a pure phase can be reached. Additionally, the influence of different Pr contents on the microstructure, phase composition, and electrical conductivity was determined. The results are discussed in terms of potential applications as a cathode electrode for SOFCs.

Experimental

Perovskite preparation

The modified sol–gel (Pechini) method was used to prepare samples of $La_{0.7-x}Pr_xCa_{0.3}MnO_3$ perovskites ($x = 0.35$, 0.49, 0.53, 0.56, 0.63 and 0.7) [38]. Precursors, lantanum (III) nitrate hexahydrate $La(NO_3)_3{\cdot}6H_2O$ (99% trace metals basis), praseodymium (III) nitrate hexahydrate $Pr(NO_3)_3{\cdot}6H_2O$ (99% trace metals basis), calcium nitrate tetrahydrate $Ca(NO_3)_2{\cdot}4H_2O$ (≥99.0%), and manganese (II) nitrate hydrate $Mn(NO_3)_2{\cdot}H_2O$ (99.99% trace metals basis) were acquired from Sigma-Aldrich. Equimolar amounts of La, Pr, Ca, and MnO_3 were weighed and dissolved in deionized water to give a concentration of 0.25 M. The solution was then acidified with 2 mL of nitric acid (HNO_3) (ACS reagent, 70%). In a next step, citric acid (ACS reagent, ≥99.5%) was also added in a 1:4 (metal:citric acid) ratio and ethylene glycol (ReagentPlus®, ≥99%) in ratio 1:10. The final solution was stirred for 5 min in an ultrasonic bath (40 kHz, Branson Ultrasonics Corporation) and heated for 4 h at 170 °C on a hot plate to generate the gel. Once the dried precursor was obtained, samples were sintered in a muffle furnace at 1000 °C for 4 h in an air atmosphere. Then, to 500 mg of the obtained powder, 0.1–0.2 mL of polyvinyl alcohol (PVA) was added as binder and it was heated at 300 °C in an oven for 30 min to be ground in an agate mortar. Finally, the powders were compacted uniaxially at 10 MPa/cm^2.

Characterization

The crystalline structure of the synthesized perovskites was determined by X-ray diffraction (XRD) using a Bruker D8 Advance diffractometer equipped with a Lynxeye detector, a K_α radiation source ($\lambda = 1.5405$ Å) at a scan rate of 0.01°, step time of 738.4 s at 35 kV and 25 mA; samples were analyzed in a 2θ range from 20° to 80°. An estimate of the crystallite size was carried out using Scherrer's equation [39]. Quantitative phase analysis based on refinement of the Rietveld structure of perovskites was carried out using the X'Pert High Score Plus V3.0e software package from PANalytical using a background polynomial of eight coefficients and 1/*X* term. The models were obtained from the database of the same program. The parameters for the phases were scale factors, unit cell, atomic coordination, and profile variables for both perovskites and oxides. It is important to mention that in the case of oxides, the atomic coordination was not refined. A pseudo-Voight function was chosen to fit the shape of the peak for the refinements in the HighScore Plus software.

Scanning electron microscopy was used to observe the microstructure of the synthesized perovskites with the SEM JEOL-6701F equipment, and the elemental analyses were also estimated by energy dispersive X-ray spectroscopy (EDS) before and after the sintering process. The surface elemental composition of the samples was analyzed with an X-ray photoelectron spectrometer with monocromatized Al Kα radiation (1486.6 eV). The base pressure of the instrument was 10^{-8} Torr. Survey scans were obtained in the 1400 to 0 eV energy range at 1.0 eV per step with a pass energy of 100 eV. In addition, high-resolution XPS scans were completed at 0.2 eV energy steps and a pass energy of 50 eV (constant pass energy mode). The full-width at half-maximum (FWHM) measurement for the Cu 2p3/2 line in the metallic state at these settings is 1.6 eV. These detailed scans were recorded for La3d, C1s, Pr3d, Mn2p, Ca2p, and O1s for the coated samples. The analyzed area of the XPS measurements was ~800 mm^2. All binding energy (BE) measurements were corrected for charging effects with reference to the C1s peak at 285.5 eV. This reference gave BE values with an accuracy of 0.2 eV. The collected data were analyzed using the Shirley background subtraction method and performed with a Gaussian-Lorentzian profile. For quantitative analysis, signal intensities were measured using the integrated area under the detected peak. To assess the atomic surface ratios, the sensitivity factors provided by the SDP v4.0 software were used and the cross-section for X-ray excitation was calculated by the Scofield method [40]. Electrical properties were carried using the four-point probe method on sintered pellets. The pellets diameter was 15.57 mm with a thickness of 1.06 mm after the sintering process at 1000 °C. Measurements were carried out with a Keithley Model 2410C by applying a DC voltage from 0.01 to 0.08 V (V_{app}) with steps of 0.01 and room temperature based on the proportional–integral derivative method. During the analysis, it was initially assumed that the tip of the probe was quite small and the resistivity could be computed as a bulk sample. Thereafter, these results were confirmed using the Van Der Pauw in Hall effect methodology using an ECOPIA HMS 3000 apparatus with a Hall field of 0.0550 T orthogonal to the measurements.

Results and discussion

Structural analysis

X-ray diffraction patterns were carried out in order to understand the effect of partial replacement of the A-site, Pr instead of La, and the structural deviation from the ideal cubic structure in ABO_3 perovskites was determined. Fig. 1 shows the XRD spectra of the as-prepared perovskites by the sol–gel based Pechini method after the sintering process at 1000 °C. As can be observed, the main intensity peaks matched well with the orthorhombic crystal system and *Pnma* space group (ICDD 98-009-2948 chart) which display the typical sharp and intense reflections of high crystallinity perovskites [41]. However, XRD spectra also show narrow signals in some compositions that

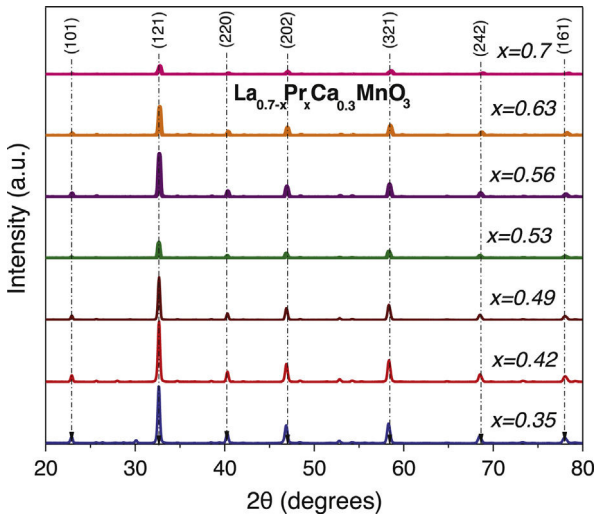

Fig. 1 – X-ray diffraction patterns of the $La_{0.7-x}Pr_xCa_{0.3}MnO_3$ synthesized perovskites after sintering process at 1000 °C for 4 h.

could indicate the appearance of another phase. To confirm this assumption, a closer view of these patterns in the 20–35° range was carried out. Fig. 2a–g shows compositions in which other oxide compounds were identified; i.e. when La substitutions were between 0.35 and 0.49. These peaks matched with PrO_2 (ICDD 06-0410 chart), and La_2O_3 (ICDD 83-1348 chart $a = b = 0.373$ nm, $c = 0.6129$ nm) which crystallize in the cubic and hexagonal phases [42–44]. It is evident that the intensity of the secondary phases (impurities) tends to decrease with the substitution of the La ion. However, under the experimental conditions of the Pechini method, only pure perovskites with two atomic compositions of Pr ($x = 0.53$ and 0.70) can be obtained, which coincide with an orthorhombic crystal system and a *Pnma* space group. The formation of secondary phases negatively influences the ionic conductivity of SOFC operation due to decreased interparticle densification affecting the triple phase boundary.

The Pechini method has been previously reported to synthesize different perovskites using citric acid and low temperatures in comparison with solid state reaction, but it reported considerable quantities of undesirable impurities (secondary phases) that require further treatment to reduce them [38]. In addition, the obtaining of $Pr_{0.7}Sr_{0.3}Mn_{0.9}Cr_{0.1}O_3$ has been reported in the absence of impurities when a calcined process above 850 °C is applied [45]. Then, although sintering temperature plays an important role in reducing secondary phases, it can be conditioned by structural incorporation in the A-site (lattice) for other types of rare earths in combination with the synthesis method. The crystallite size of the synthesized perovskites was estimated by the Scherrer's equation $d_{nm} = (k\lambda)/(\beta \cos\theta)$. In this formula, d_{nm} is the crystallite size in nm, λ is the wavelength of the X-ray, β is the full-width at half-maximum, k is the shape factor, and θ is the Bragg's angle of diffraction. The estimation of the crystallite size was realized as an average of the three main intensity planes; (1 2 1), (2 0 2) and (3 2 1) and the results with their corresponding standard deviation are shown in Fig. 3. The addition of Pr in the ABO_3 perovskite shows a gradual increase in the crystallite size from 27.6 nm ($x = 0.35$) to 33.2 nm ($x = 0.56$) and began to reduce with a partial substitution of $x = 0.63$ (32.6) up to obtain a small crystallite size of 24.2 nm with a total lanthanum substitution in the A-site, $Pr_{0.7}Ca_{0.3}MnO_3$.

To confirm the existence of pure phases, a refinement of the structure was realized on the XRD spectra of the samples by the Rietveld method. Fig. 4a–e shows the refinement of the perovskites with an atomic substitution between 0.49 and 0.70. The analysis was initially carried out considering the atomic position of La_2O_3 and/or PrO_2 as secondary phases and LPCM as the main structure. However, the Rietveld refinement confirms that except for a composition of $x = 0.53$ and 0.70, the other compositions fit well only when a secondary phase is considered in the analysis. Thus, although samples with a Pr amount of 0.35, 0.49, 0.56 and 0.63 present a main orthorhombic structure, small lattice reflections of other symmetry inevitably also appear; whereas samples with a composition of 0.53 and 0.7 matched well with a pure phase of an ABO_3 perovskite that belong to *Pnma* space group. The calculated parameters showed adequate values ensuring an adequate fitting between experimental–theoretical data, Table 1. The goodness of fit was obtained under ($\chi^2 \leq 10$) validating the analysis with the used software. Some differences in the unit cell parameters, atomic coordination and the site occupancy were observed for oxygen (O1), calcium (Ca), praseodymium (Pr), and lanthanum (La), depending on La substitution, but not clear trend was observed in this parameter. However, the cell volume tends to decrease as the amount of Pr is increased from 231.703 to 228.904 Å^3, which is in agreement with the crystallite size and the obtaining of a pure phase. In comparison to other perovskites with lower amounts of Pr, such as those reported by Luque et al. ($La_{0.325}Pr_{0.30}Ca_{0.375}MnO_3$) [46], the unit cell parameters are higher than those observed in the analysis, but the R_{wp} was lower, suggesting a better fit. The stability of the perovskite was analyzed in terms of the Goldsmith tolerance factor $t = (r_A + r_o)/(\sqrt{2}(r_B + r_o))$. This factor indicates stability in the ceramic materials when it is found in the following range $0.77 \leq t \leq 1.0$ and depends on the ionic radio of the ions (cation and anions) [47]. The obtained perovskites presented a distortion degree close to 0.890, confirming that the samples present a stable structure. The orthorhombic distortion is characterized by a deformation that occurs with the growth of the formation of the net, and meet the relation $c/\sqrt{2} \leq a \leq b$. This deformation is carried out through Jahn-Teller distortion with a clear elongation in the *b*-axis. It can be also observed that *b* and *c* lattice parameter decreased with the amount of Pr and in consequence *c*/*a* and $\sqrt{2}c/b$ ratios are close to 1, confirming the final symmetry determined during the Rietveld analysis. These results represented a variation in the site occupancy that is reflected in a correlation between the site occupancy and the atomic quantity of these elements. Previously, it has been reported similar differences in the lattice parameters, for example synthesized perovskites based on $Ca_{1-x}Gd_xMnO_3$ [48] and $Gd_{1-x}Sr_xMnO_3$ (GSMO) ($0.2 \leq x \leq 0.5$) [49] had differences between *a* and *c* parameters, suggesting that Jahn-Teller distortion take places by the presence of doping them with Mn^{3+} ion in the octahedral environment. In other works, the volume of the unit cell also decreased with an increase in the *x* content, mainly due to the distortion by

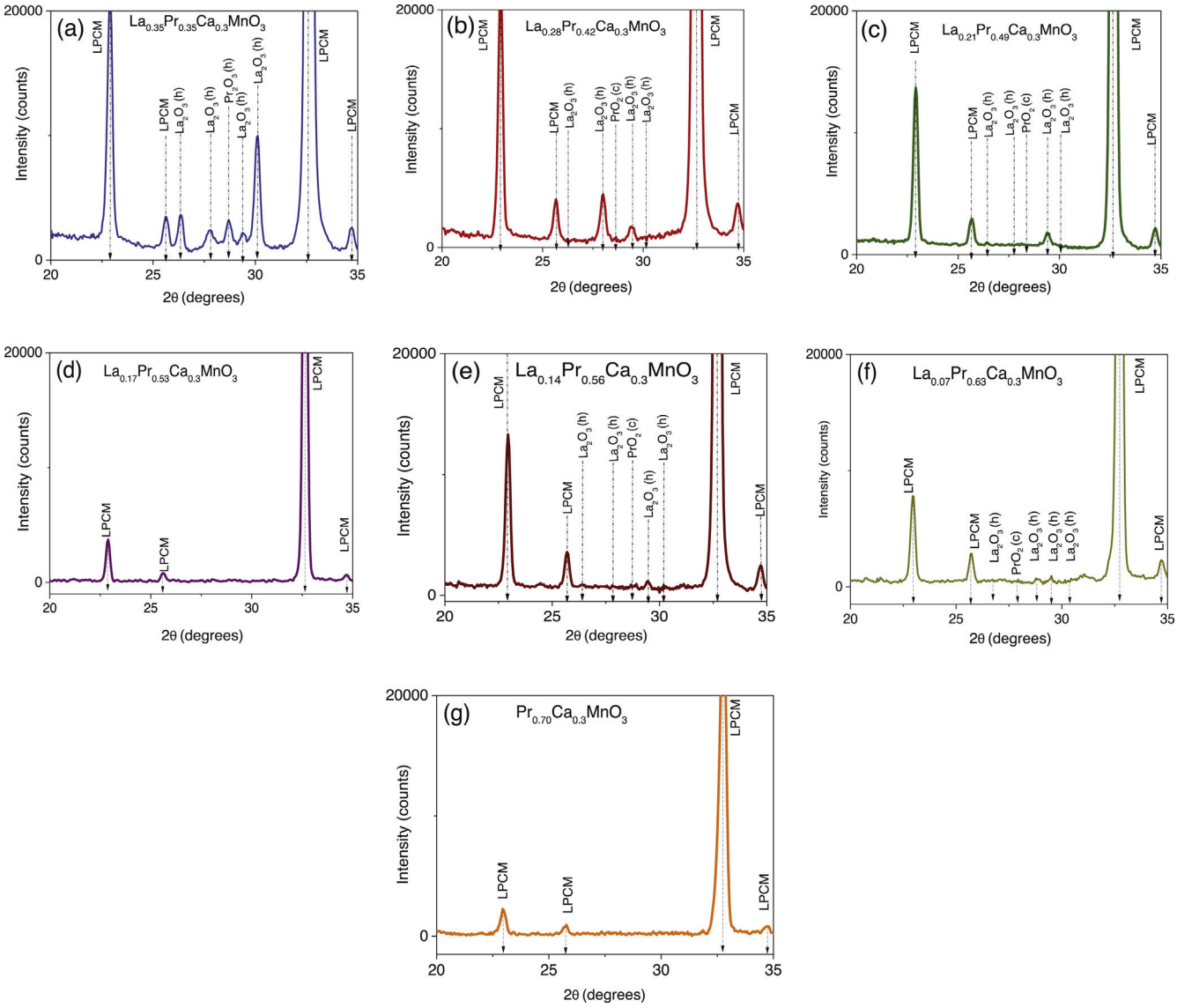

Fig. 2 – XRD patterns between 20 and 35 degrees of the synthesized perovskites (a) $La_{0.35}Pr_{0.35}Ca_{0.3}MnO_3$, (b) $La_{0.28}Pr_{0.42}Ca_{0.3}MnO_3$, (c) $La_{0.21}Pr_{0.49}Ca_{0.3}MnO_3$, (d) $La_{0.17}Pr_{0.53}Ca_{0.3}MnO_3$, (e) $La_{0.14}Pr_{0.56}Ca_{0.3}MnO_3$, (f) $La_{0.14}Pr_{0.56}Ca_{0.3}MnO_3$ and (g) $Pr_{0.70}Ca_{0.3}MnO_3$.

the deficit of cations A, B and oxygen, which is in agreement with our synthesized perovskites.

Morphological studies

To evaluate the effect of the sintering process on the porosity and either agglomeration or uniform grain formation, SEM measurements were performed on $La_{0.7-x}Pr_xCa_{0.3}MnO_3$ samples before and after the sintering process was performed at 1000 °C (Fig. 5a–g). The morphological aspects of the samples, before the sintering process, display irregular micro-semispherical grains with high spacing between them (porosity); while the calcined specimens at 1000 °C showed a densification with the typical cauliflower-like morphology [50], significantly reducing the porosity. This type of morphology has been previously observed in different perovskites such as $SrFeO_{\sim 2.85}$ where the increase in size and decrease in porosity were mainly attributed to the increase in calcination temperature [38]. In particular, the densification and grain size variation in the as-obtained ABO_3 perovskites are also influenced by the Pr content, which can be correlated with the differences in ionic radii between La and Pr. A similar behavior has been previously observed for strontium-doped lanthanum manganite perovskites [50]. The porosity volume percentage in the samples was estimated, finding the following variation: 15% (0.35), 14% (0.42), 15% (0.49), 13% (0.53), 12% (0.56), 10% (0.63) and 8% (0.70). Previously, the influence of the sintering temperature in different perovskites for stoichiometric compositions has been studied, where it has been shown that an adequate treatment to achieve the densification of green pellets is above 1000 °C, therefore the remained porosity observed in this study can be avoided with temperatures around 1500 °C [51]. In our research group, thermogravimetric and thermal expansion coefficient measurements of $La_{0.7-x}Pr_xCa_{0.3}MnO_3$

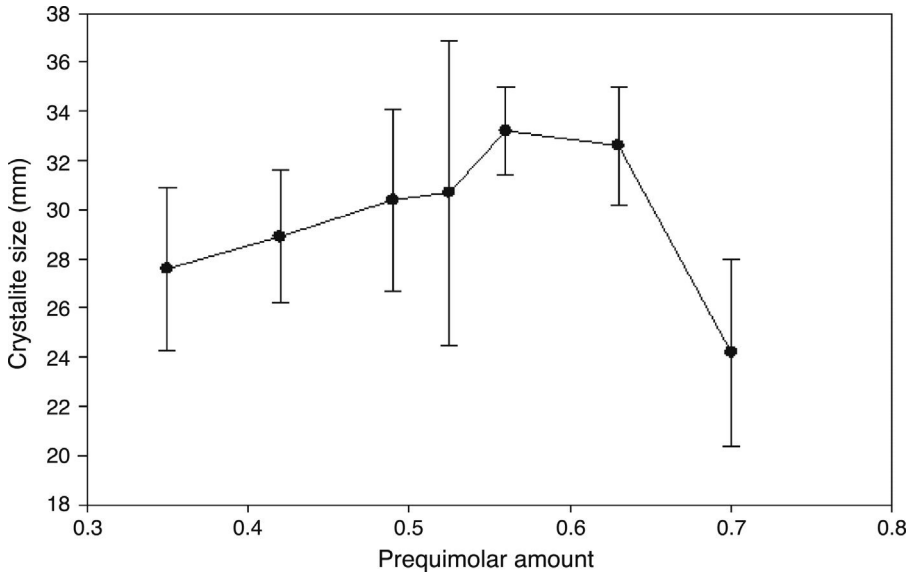

Fig. 3 – Relation between the atomic amount of Pr and the crystallite size of the synthesized $La_{0.7-x}Pr_xCa_{0.3}MnO_3$ perovskites.

Table 1 – Summary of structural and refinement parameters of $La_{0.7-x}Pr_xCa_{0.3}MnO_3$ perovskites.

x	0.49	0.53	0.56	0.63	0.7
System	Orthorhombic				
Space group	*Pnma*				
a (Å)	5.470	5.467	5.475	5.470	5.477
b (Å)	7.726	7.718	7.716	7.703	7.686
c (Å)	5.481	5.477	5.466	5.451	5.436
$c/\sqrt{2}$	3.8756	3.8728	3.8650	3.8544	3.8438
c/*a*	1.0020	1.0018	0.9983	0.9965	0.9925
$\sqrt{2}c/b$	1.0032	1.0037	1.0016	1.0007	1.0002
$\alpha = \beta = \gamma$	90	90	90	90	90
R_{exp}	2.594	4.920	3.082	3.670	6.460
R_p	7.917	17.533	6.580	10.350	19.432
R_{wp}	8.049	13.668	4.910	8.655	13.595
Goodness of fit (χ^2)	9.623	7.716	2.543	5.561	4.428
Cell volume (Å^3)	231.703	231.010	230.994	229.765	228.904
		O			
X	0.2840	0.2841	0.2840	0.2840	0.3110
Y	0.0400	0.0366	0.0369	0.0369	0.0208
Z	0.2887	0.2839	0.2826	0.2826	0.3067
		Ca			
X	0.0241	0.0139	0.0289	0.0029	0.0290
Z	0.0058	0.0013	0.0045	0.0013	0.0013
SOF	0.3	0.3	0.3	0.3	0.3
		Pr			
X	0.0255	0.0256	0.0319	0.0290	0.0294
Z	0.0016	0.0007	0.0013	0.0013	0.0001
SOF	0.49	0.5126	0.5600	0.6277	0.6904
		La			
X	0.0231	0.0252	0.0097	0.0290	0.0290
Z	0.0012	0.0043	0.0152	0.0013	0.0013
SOF	0.21	0.1863	0.14	0.0677	0
Distortion degree (*t*)	0.891	0.890	0.888	0.885	0.883

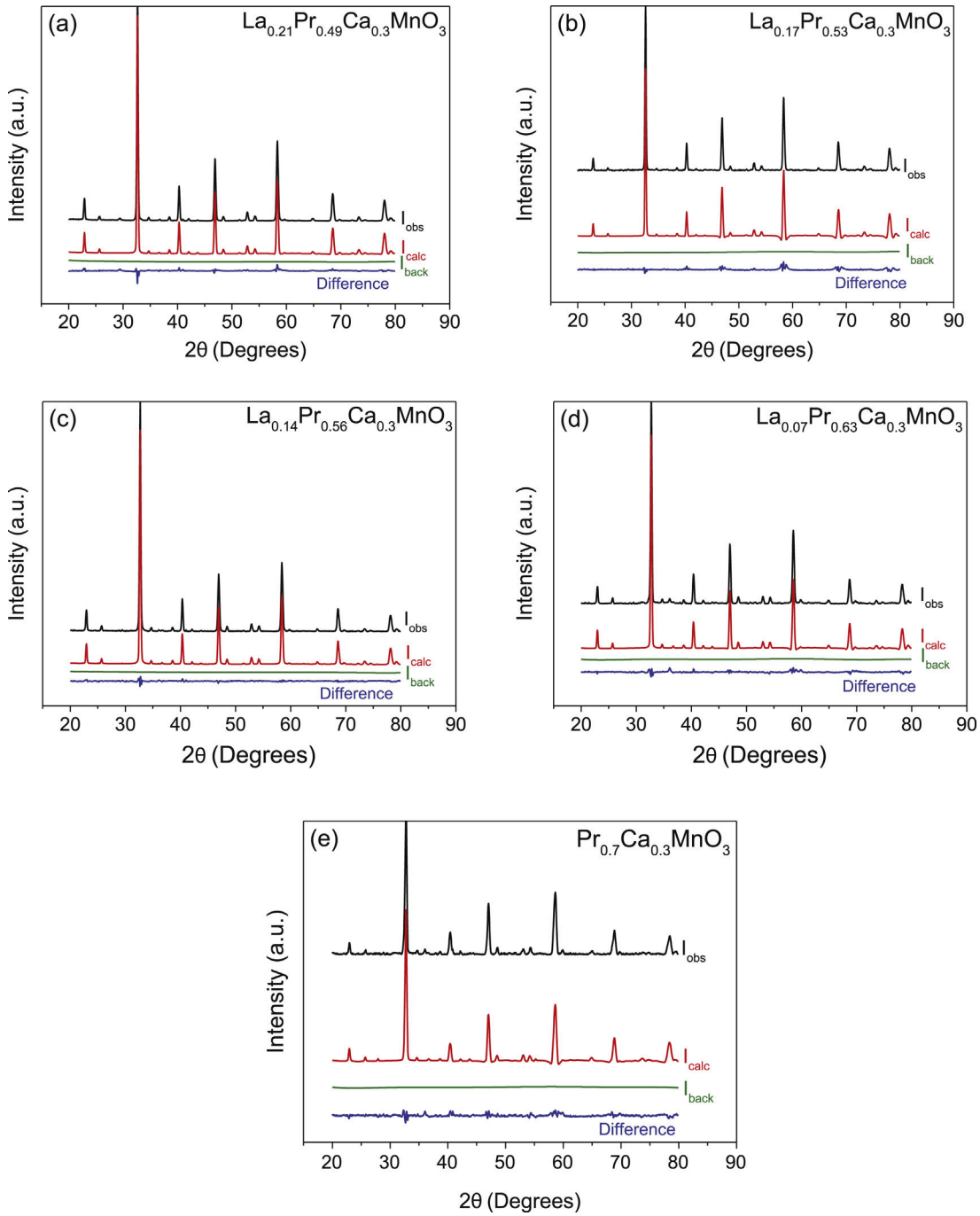

Fig. 4 – XRD patterns and Rietveld refinement of the perovskites (a) $La_{0.21}Pr_{0.49}Ca_{0.3}MnO_3$, (b) $La_{0.175}Pr_{0.525}Ca_{0.3}MnO_3$, (c) $La_{0.14}Pr_{0.56}Ca_{0.3}MnO_3$, (d) $La_{0.07}Pr_{0.63}Ca_{0.3}MnO_3$ and (e) $Pr_{0.7}Ca_{0.3}MnO_3$.

perovskites were previously reported in the temperature range of 25–1000 °C for a different synthesis method, indicating that sintered pellets at 1000 °C have sufficient densification and chemical compatibility with yttria stabilized zirconia (YSZ) to be used as a cathode electrode for SOFCs. It was also determined that the amount of Pr in the perovskite favors the similarity with the thermal expansion coefficient between the cathode and the electrolyte (YSZ) [34]. According to these works, the porosity of the samples obtained by the Pechini method can be formed during the synthesis process (powders), as a result of a rapid release of gases during the initial drying process. Subsequently, with the calcination process, the grains become larger with a cauliflower-like shape increasing the degree of densification due to the rupture of the pore wall [52]. Then, considering an ionic diffusion pathway, the particles were melted and fused depending on both

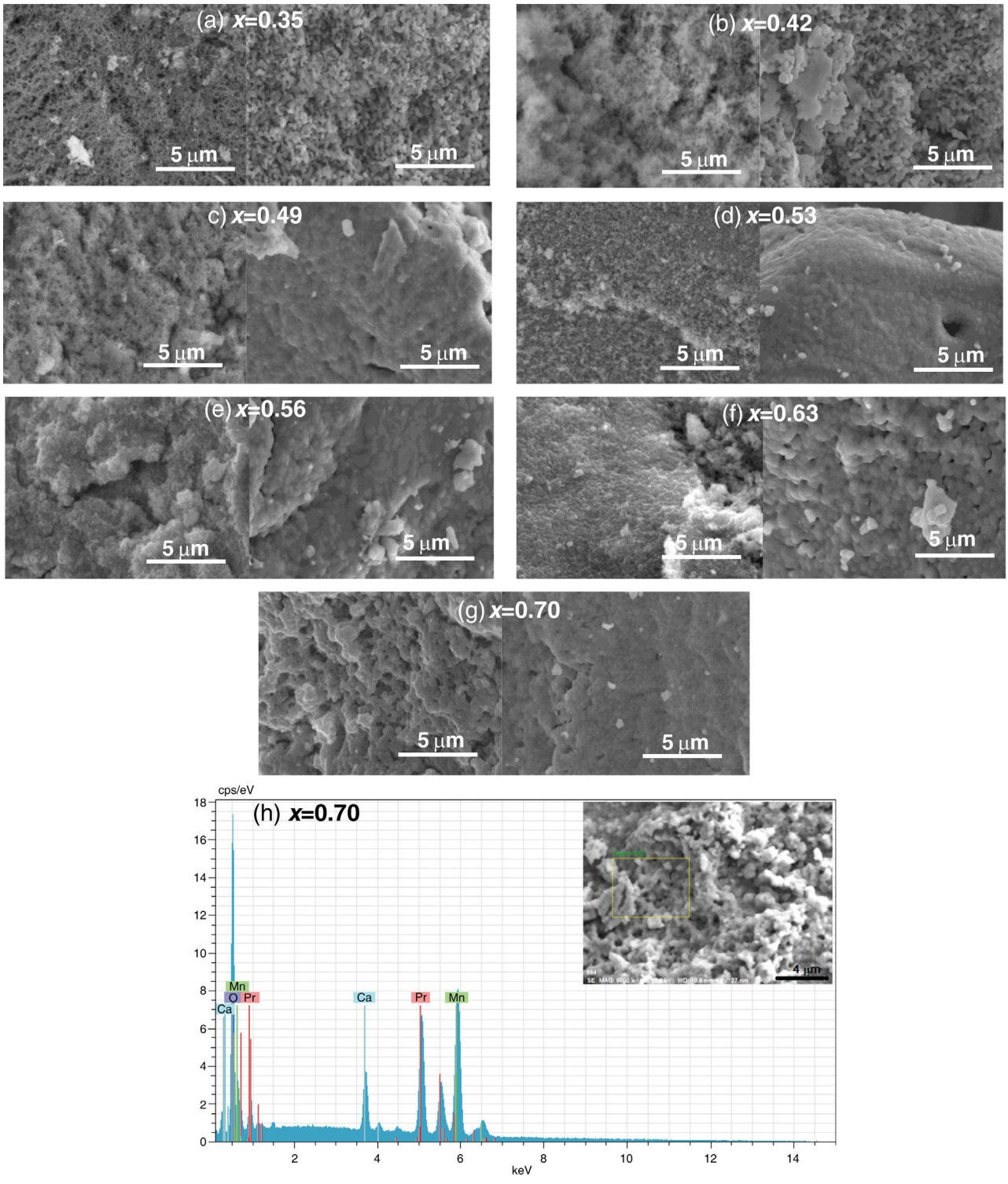

Fig. 5 – SEM images of the $La_{0.7-x}Pr_xCa_{0.3}MnO_3$ perovskites before and after the sintering process at 1000 °C, (a) 0.35, (b) 0.42, (c) 0.49, (d) 0.53, (e) 0.56, (f) 0.63 and (g) 0.70. (h) Selected EDS spectra of the perovskites with a composition $x = 0.70$. Images within the graph display the SEM images indicating the selected area for EDS analysis.

calcination temperature and Pr content. In this way, granular growth occurs in a three-dimensional aligned manner to form large agglomerates.

The elemental composition of the samples was analyzed by energy dispersive spectroscopy (EDS). Fig. 5h shows a representative EDS spectra for $La_{0.7-x}Pr_xCa_{0.3}MnO_3$ perovskites that crystallized in a pure phase ($x = 0.7$). The area selected for analysis confirmed the presence of Pr, Ca, Mn and O without contaminants; which can also be observed for other compositions in the supplementary material (Figs. S1–S3).

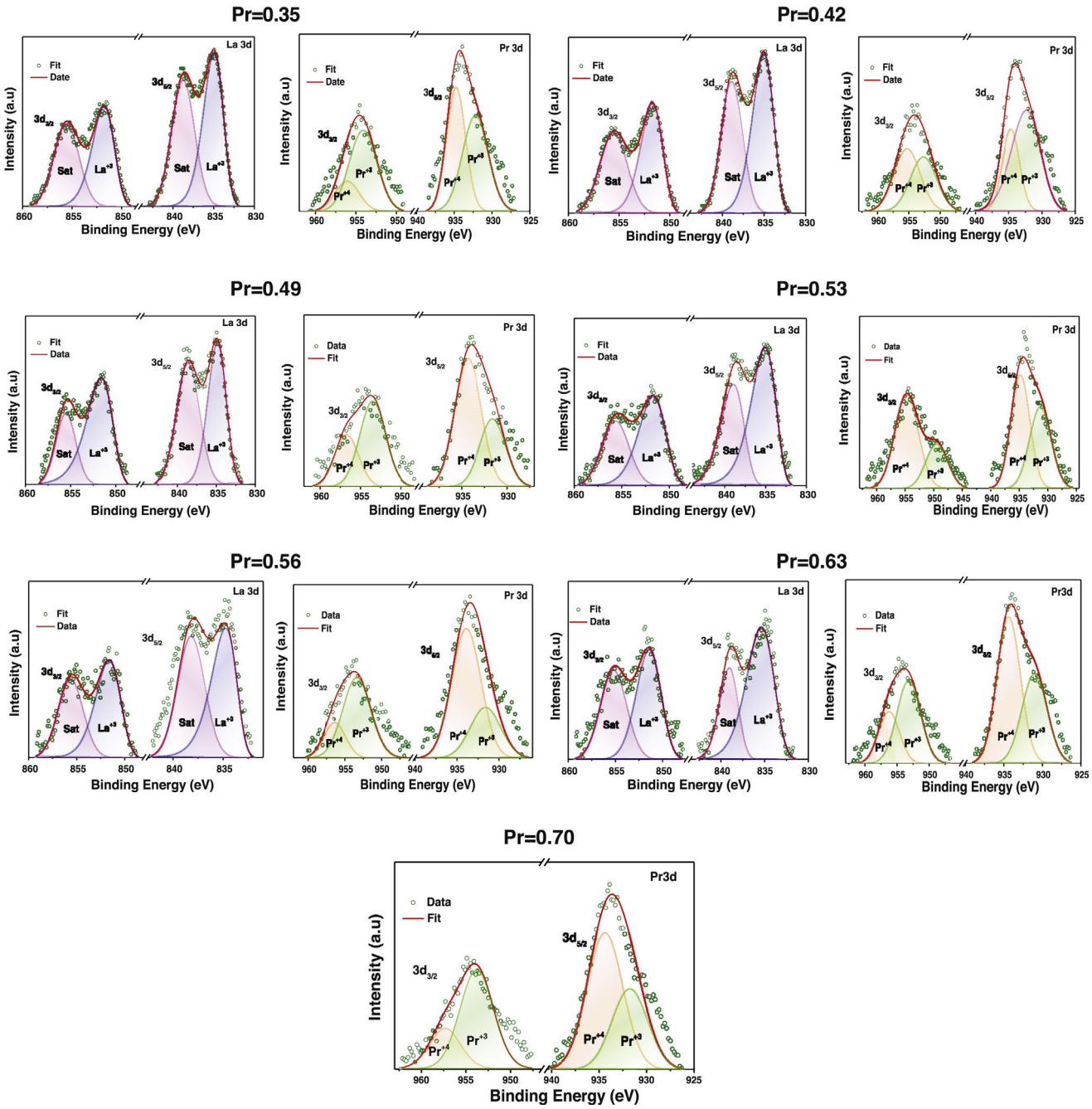

Fig. 6 – XPS of the perovskites in the La3d and Pr3d regions using different compositions of the Pr cation. The figure identifies the characteristic satellite (sat) peaks correlated with physical interactions during the La and Pr photoemission process.

To quantitatively determine the composition of the samples, XPS analyses were performed and are discussed below.

Chemical composition

The chemical composition of the as-prepared samples XPS measurements was analyzed in pellets after the sintering process at 1000 °C. The oxygen vacancy concentration, the oxidation states of the metal ions, Pr^{4+}/Pr^{3+} and Mn^{3+}/Mn^{4+} ratios that condition the distortion in the orthorhombic structure, and the electrochemical performance was also analyzed through XPS fitting.

Figs. 6 and 7 show experimental XPS spectra as a function of the La substitution with its corresponding adjustment to determine the atomic percentage corresponding to its different electronic states. The lanthanum deconvolution presents traditional peaks in 3d core level spectra ($3d_{3/2}$ and $3d_{5/2}$). Small displacements were observed in the binding energies with the amount of Pr as a consequence of the variation of the peaks shape. It is known that La and Pr are hygroscopic

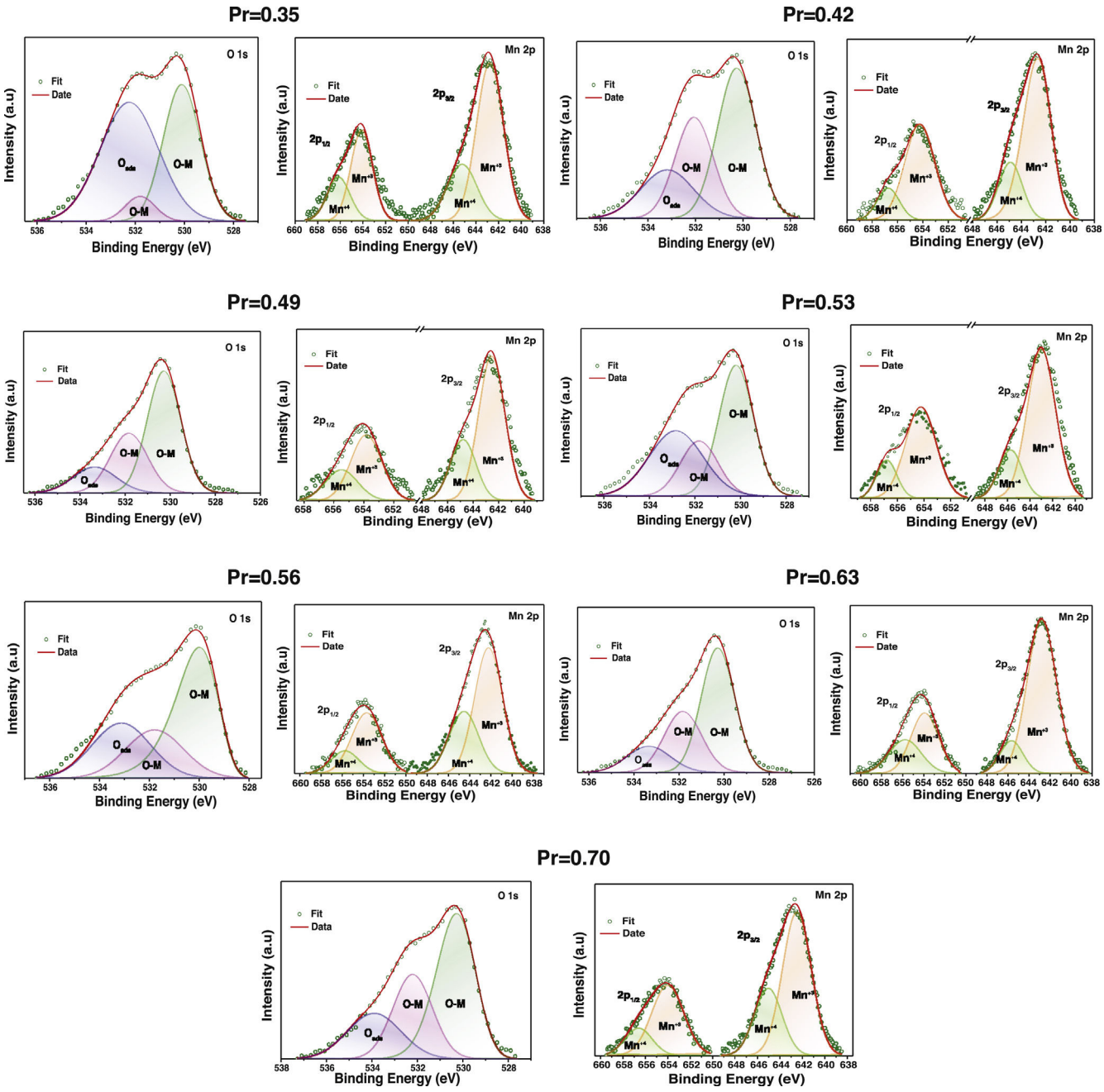

Fig. 7 – XPS of the perovskites in the O1s and Mn2p regions using different compositions of the Pr cation.

in nature and the formation of oxide–hydroxide compounds and the changes in the composition can explain the observed variations [53]; however, the La doublets with their corresponding satellite maintain a known difference of ~17 eV. On the other hand, praseodymium presents two oxidation states Pr^{3+} and Pr^{4+} in the $3d_{3/2}$ and $3d_{5/2}$ core levels (Fig. 6). The $Pr3d_{3/2}$ core level (~954.52 eV) presented the highest ratio of Pr^{3+}, whereas an inverse trend was obtained in the $Pr3d_{5/2}$ core level (~934.14 eV). The energy separation between both peaks of ~20.5 eV is in agreement with previous observations [54]. The Pr^{3+}/Pr^{4+} ratio tends to decrease with the addition of Pr, which is more evident between $x = 0.35$ (1.64) and $x = 0.53$ (0.59) and from there it begins to increase between 0.56 (1.06) and 0.70 (1.17). Then, a rise in the quantity of Pr^{4+} species will cause an increase in electrical performance [55]. The Mn2p core level showed two asymmetric peaks ($2p_{1/2}$ @~654.22 eV and $2p_{3/2}$ @~642.89 eV) that fit well with two oxidation states of manganese (Mn^{3+} and Mn^{4+}) (Fig. 7). The high peaks during deconvolution correlated with Mn^{3+} ions and the other couple to the Mn^{4+} ions, confirming the coexistence of the two oxidizing states [56].

The variation of the binding energies depending on the Pr amount can be observed in Table 2. The Mn^{3+}/Mn^{4+} atomic ratios varied from 2.18 ($x = 0.35$) to 3.68 ($x = 0.53$), indicating that La substitution by Pr ions promotes the hole doped system instead of the electron system; this ratio increases with

Table 2 – Cationic ratios for the $La_{0.7-x}Pr_xCa_{0.3}MnO_3$ perovskites.

Cationic ratios	$La_{(0.7-x)}Pr_{(x)}Ca_{0.3}MnO_3$ (x)						
	0.35	0.42	0.49	0.53	0.56	0.63	0.70
Pr^{3+}/Pr^{4+}	1.64	1.29	097	0.59	1.06	1.07	1.17
Mn^{3+}/Mn^{4+}	2.18	3.68	2.23	3.68	2.34	2.72	2.58
La/Mn	0.47	0.41	0.36	0.23	0.12	0.11	–
(La + Pr)/Mn	0.83	0.89	0.72	0.62	0.41	0.53	0.49
Pr/Mn	0.36	0.48	0.36	0.39	0.28	0.40	0.49
La/Pr	1.30	0.86	1.03	0.59	0.44	0.32	–
Pr^{3+}/Mn^{3+}	0.91	0.72	0.72	0.47	0.74	0.71	0.75
Pr^{4+}/Mn^{4+}	1.20	2.04	1.63	2.94	1.62	1.80	1.65
La/Ca	4.47	2.39	2.00	1.04	0.86	0.64	–
Pr/Ca	3.43	2.77	1.95	1.76	1.96	1.99	2.14
Ca/Mn	0.10	0.17	0.18	022	0.14	0.20	0.23

Table 3 – Electrical measurements of $La_{0.7-x}Pr_xCa_{0.3}MnO_3$ perovskites at room temperature.

$La_{(0.7-x)}Pr_{(x)}Ca_{0.3}MnO_3$ (x)	Charge carrier density (η, m^{-3})	Mobility (μ) ($m^2\,V^{-1}\,s^{-1}$)	ρ (Ω m)	Conductivity ($S\,m^{-1}$)	ρ (Ω m)	Conductivity ($S\,m^{-1}$)
	Hall effect				Four-point Kevin probe	
0.35	−5.54E+12	4.42E−05	0.0462	21.64	0.0235	42.55
0.42	1.10E+12	8.79E−05	0.0425	23.53	0.0134	74.62
0.49	1.09E+13	7.59E−05	6.09E−03	164.00	9.66E−03	103.51
0.53	−4.12E+13	8.87E−05	5.41E−03	184.84	7.97E−03	125.47
0.56	−4.19E+13	6.05E−05	5.80E−03	172.41	9.36E−03	106.83
0.63	1.64E+14	1.94E−04	7.52E−3	132.97	0.0105	95.23
0.70	−1.07E+19	3.08E−05	0.0156	64.10	9.82E−03	101.83

substitution of La. Thus, the appearance of Mn^{4+} species is mainly due to manganese oxidation and/or charge compensation in the perovskite base structure ($LaMnO_{3\pm\delta}$) during lanthanum substitution, causing oxygen loss. In general, La/Mn, La/Ca and (La + Pr)/Mn ratios are reduced with the amount of Pr; although some specific compositions show a contrary tendency. Other cationic ratios such as Pr^{3+}/Mn^{3+}, Pr^{4+}/Mn^{4+} Ca/Mn displayed values related to the lanthanum substitution. Then, the discrepancy has been previously observed in different perovskites and attributed to Mn enrichment during La substitution by a migration of lanthanum to the surface.

O1s spectra which were deconvoluted into three peaks referring to chemisorbed oxygen (O_{ads}), ~532.2 eV, and lattice oxygen (O–M), ~531.7 and ~530.1 [57]. Adsorbed oxygen species are known to promote the reactivity at the surface of electrode materials and the redox process. Therefore, the fact that the proportion of the O–M species is higher than the O_{ads} and that this varies positively with the Pr substitution is consistent with the compute Mn^{3+}/Mn^{4+} ratio [58]. The surface composition is in good agreement with the theoretical calculation (see supplementary material).

Electrical measurements

The electrical conductivity of the electrode materials is influenced by the crystal structure; therefore, to explain changes in these properties with the Pr composition and to evaluate whether the synthesized materials can be considered as suitable materials for solid state fuel cells (SOFCs), the four-point probe method was evaluated after the sintering process at room temperature. The methodology contemplates an equidistant spacing between points, c.a. 0.04 inches (0.1016 cm), so the resistance value was calculated by linear interpolation and multiplied by the factor $2\pi S = 0.638372$ cm. The thickness of the pellets used was 1.06 mm with a diameter of 15.57 mm. The resistivity and conductivity values as a function of lanthanum substitution can be observed in Table 3. The obtained measurements showed an increase in conductivity as the Pr content increased between 0.35 and 0.53, reaching a maximum value of 125.47 $S\,m^{-1}$, and began to decrease with a greater Pr amount, between $x = 0.56$ (106.83 $S\,m^{-1}$), and $x = 0.63$ (95.23 $S\,m^{-1}$). Finally, when a total substitution of La was made, the electrical conductivity of the electrode material increased again up to reach a value of 101.83 $S\,m^{-1}$. The variations can be related to the differences in the observed phases and the (La + Pr)/Mn ratio. The highest electrical conductivity is lower than that reported for other types of electrode materials such as $La_{1-x}Ca_xFe_{0.9}Mn_{0.1}O_{3-\delta}$ (100 $S\,cm^{-1}$) [59] or $La_{0.9}Sr_{0.1}M_{0.9}Mg_{0.1}O_{2.9}$ (M = Al, Ga, Sc, In) with values of 95 $S\,cm^{-1}$ or 180 $S\,cm^{-1}$ [59], although the values obtained in this work (42.55–125.47 $S\,m^{-1}$) may present a mixed behavior of ionic–electronic conductivity with the temperature as found for the perovskites of $La_{0.9}Sr_{0.1}Al_{0.9}Mg_{0.1}O_{2.9}$ [60] and $La_{0.9}Sr_{0.1}Sc_{0.9}Mg_{0.1}O_{2.9}$ (50–130 $S\,m^{-1}$) [61]. To confirm this assumption, an analysis of the charge carriers as a function of the Pr amount was performed by the Hall effect method combined with a resistivity measurement at room temperature. It is important to note that silver dye was used during

the measurements to ensure contact in the system with a cloverleaf configuration.

The Hall effect is used to determine the charge carrier density (η), depending on the sign, the electrode can be ascribed as *n* or *p*; that is, acceptor of electrons ($\eta > 0$) or increase the electrons for conduction, donor of electrons ($\eta < 0$). The Hall effect results indicate that electrical conductivity can be generated in both *p* and *n*-type carriers (Table 3); that is, they can conduct ionically and electronically in a mixed manner. On the other hand, the electrical characterization using the Van der Pauw technique showed a similar trend to that obtained by the four-point method, and the differences between them may be related to the characteristics of each technique. Thus, the samples that presented the highest electrical conductivity are samples with an atomic composition of 0.53 (184.84 S m^{-1}) and acceptor character. The correlation with the electrical properties suggests that a combination of the Pr amount and the pure phase obtained in the perovskite synergistic influences the electrical performance. It is also clear that higher Pr amounts favored electron transport, which can positively be used in the performance of cathode for SOFCs.

Conclusions

This paper reports the production of $La_{0.7-x}Pr_xCa_{0.3}MnO_3$ perovskites by lanthanum substitution through the simple Pechini sol–gel method. Several compositions were analyzed ($x = 0.35$, 0.49, 0.53, 0.56, 0.63 and 0.7) to determine the effect of Pr amount on the structural, morphological, and electrical parameters as a potential application in SOFCs. All the synthesized $La_{0.7-x}Pr_xCa_{0.3}MnO_3$ perovskites match the orthorhombic crystal system and the *Pnma* space group. The substitution of lanthanum by atomic percentage of Pr caused the formation of small peaks corresponding to secondary phases of Pr and La oxides ($x = 0.35$, 0.49, 0.56 and 0.63), while the pure phases were obtained with a partial substitution of Pr at 0.53 and complete substitution to obtain $Pr_{0.7}Ca_{0.3}MnO_3$ perovskites, which was confirmed by Rietveld refinement. Depending on the size of the crystallites, the cell volume tends to decrease with the atomic percentage of Pr. The addition of Pr in the perovskite is characterized by an orthorhombic Jahn-Teller distortion with a clear elongation in the *b*-axis. The Mn^{3+}/Mn^{4+} atomic ratios ranged from 2.28 ($x = 0.35$) to 3.69 ($x = 0.53$), promoting the hole doped system instead of the electron system. Although the electrical conductivity at room temperature is low compared to previous work, the substitution of Pr by this method promotes mixed ionic–electronic conduction. The sample that showed the highest electrical conductivity is the one with an atomic weight of $x = 0.53$ (184.84 S m^{-1}) with an acceptor character, which can potentially be used as a cathode in SOFCs for energy production.

Acknowledgements

The authors are thankful for the financial support provided by Instituto Politécnico Nacional through the SIP projects: 2023-0839, 2023-0842, 2023-0348, 2023-1159, 2023-1159 and COFAA. This work has also been funded by CONACYT through project CB-2015-252181 and SNII.

Appendix A. Supplementary data

Supplementary data associated with this article can be found, in the online version, at doi:10.1016/j.bsecv.2023.09.001.

REFERENCES

[1] D. Shin, J.H. Nam, An effectiveness model for electrochemical reactions in electrodes of intermediate-temperature solid oxide fuel cells, Electrochim. Acta 171 (2015) 1–6, http://dx.doi.org/10.1016/j.electacta.2015.04.171.

[2] W. Li, Y. Cheng, Q. Zhou, T. Wei, Z. Li, H. Yan, Z. Wang, X. Han, Evaluation of double perovskite $Sr_2FeTiO_{6-\delta}$ as potential cathode or anode materials for intermediate-temperature solid oxide fuel cells, Ceram. Int. 41 (2015) 12393–12400, http://dx.doi.org/10.1016/j.ceramint.2015.06.074.

[3] A.B. Stambouli, E. Traversa, Solid oxide fuel cells (SOFCs): a review of an environmentally clean and efficient source of energy, Renew. Sust. Energy Rev. 6 (2002) 433–455, http://dx.doi.org/10.1016/S1364-0321(02)00014-X.

[4] S. Zarabi Golkhatmi, M.I. Asghar, P.D. Lund, A review on solid oxide fuel cell durability: latest progress, mechanisms, and study tools, Renew. Sust. Energy Rev. 161 (2022) 112339, http://dx.doi.org/10.1016/j.rser.2022.112339.

[5] Q. Yang, D. Tian, R. Liu, H. Wu, Y. Chen, Y. Ding, X. Lu, B. Lin, Exploiting rare-earth-abundant layered perovskite cathodes of $LnBa_{0.5}Sr_{0.5}Co_{1.5}Fe_{0.5}O_{5+\delta}$ (Ln = La and Nd) for SOFCs, Int. J. Hydrog. Energy 46 (2021) 5630–5641, http://dx.doi.org/10.1016/j.ijhydene.2020.11.031.

[6] J.-S. Shin, M. Saqib, M. Jo, K. Park, K.M. Park, J.S. Ahn, H.-T. Lim, J.-Y. Park, Degradation mechanisms of solid oxide fuel cells under various thermal cycling conditions, ACS Appl. Mater. Interfaces 13 (2021) 49868–49878, http://dx.doi.org/10.1021/acsami.1c13779.

[7] U. Anjum, T.S. Khan, M. Agarwal, M.A. Haider, Identifying the origin of the limiting process in a double perovskite $PrBa_{0.5}Sr_{0.5}Co_{1.5}Fe_{0.5}O_{5+\delta}$ thin-film electrode for solid oxide fuel cells, ACS Appl. Mater. Interfaces 11 (2019) 25243–25253, http://dx.doi.org/10.1021/acsami.9b06666.

[8] S. Yoo, A. Jun, Y.-W. Ju, D. Odkhuu, J. Hyodo, H.Y. Jeong, N. Park, J. Shin, T. Ishihara, G. Kim, Development of double-perovskite compounds as cathode materials for low-temperature solid oxide fuel cells, Angew. Chem. Int. Ed. 53 (2014) 13064–13067, http://dx.doi.org/10.1002/anie.201407006.

[9] L. Fan, B. Zhu, P.-C. Su, C. He, Nanomaterials and technologies for low temperature solid oxide fuel cells: recent advances, challenges and opportunities, Nano Energy 45 (2018) 148–176, http://dx.doi.org/10.1016/j.nanoen.2017.12.044.

[10] C.C. Wang, S. Darvish, K. Chen, B. Hou, Q. Zhang, Z. Tan, Y. Zhong, S.P. Jiang, Combined Cr and S poisoning of $La_{0.8}Sr_{0.2}MnO_{3-\delta}$ (LSM) cathode of solid oxide fuel cells, Electrochim. Acta 312 (2019) 202–212, http://dx.doi.org/10.1016/j.electacta.2019.04.116.

[11] J. Ramírez-Hernández, A.M. Torres-Huerta, S.B. Brachetti-Sibaja, M.A. Domínguez-Crespo, D. Palma-Ramírez, A.E. Rodríguez-Salazar, A. Ezeta-Mejia, $La_{0.7-x}Ln_xCa_{0.3}MnO_3$ (Ln = ProrSm) perovskites as electrode materials for SOFCs, Ceram. Int. 48 (2022) 21221–21234, http://dx.doi.org/10.1016/j.ceramint.2022.04.031.

[12] T. Ghorbani-Moghadam, A. Kompany, M. Golmohammad, The comparative study of doping Cu and Fe on the cathodic properties of $La_{0.7}Sr_{1.3}CoO_4$ layered perovskite compound: to

be used in IT-SOFC, J. Alloys Compd. 926 (2022) 166928, http://dx.doi.org/10.1016/j.jallcom.2022.166928.
[13] C. Gumeci, J. Parrondo, A.M. Hussain, D. Thompson, N. Dale, Praseodymium based double-perovskite cathode nanofibers for intermediate temperature solid oxide fuel cells (IT-SOFC), Int. J. Hydrog. Energy 46 (2021) 31798–31806, http://dx.doi.org/10.1016/j.ijhydene.2021.07.070.
[14] H.A. Taroco, J.A.F. Santos, R.Z. Domingues, T. Matencio, Ceramic materials for solid oxide fuel cells, in: C. Sikalidis (Ed.), Advances in Ceramics – Synthesis and Characterization, Processing and Specific Applications, IntechOpen, Rijeka, Croatia, 2011, http://dx.doi.org/10.5772/18297.
[15] L. Shen, Z. Du, Y. Zhang, X. Dong, H. Zhao, Medium-entropy perovskites $Sr(Fe_{\alpha}Ti_{\beta}Co_{\gamma}Mn_{\zeta})O_{3-\delta}$ as promising cathodes for intermediate temperature solid oxide fuel cell, Appl. Catal. B: Environ. 295 (2021) 120264, http://dx.doi.org/10.1016/j.apcatb.2021.120264.
[16] Z. Han, J. Bai, X. Chen, X. Zhu, D. Zhou, Novel cobalt-free $Pr_2Ni_{1-x}Nb_xO_4$ (x = 0, 0.05, 0.10, and 0.15) perovskite as the cathode material for IT-SOFC, Int. J. Hydrog. Energy 46 (2021) 11894–11907, http://dx.doi.org/10.1016/j.ijhydene.2021.01.045.
[17] C. Zener, Interaction between the d shells in the transition metals, Phys. Rev. 81 (1951) 440–444, http://dx.doi.org/10.1103/PhysRev.81.440.
[18] N. Kouki, A. Guedri, S. Hcini, A. Algreiby, R. Charguia, R.K. Alharbi, Structural, magnetic, magnetocaloric and critical studies of Sm-substituted $La_{0.67-x}Sm_xPb_{0.13}Ca_{0.2}MnO_3$ perovskite manganites, Solid State Commun. 363 (2023) 115104, http://dx.doi.org/10.1016/j.ssc.2023.115104.
[19] D. Pchelina, V. Sedykh, N. Chistyakova, V. Rusakov, Y. Alekhina, A. Tselebrovskiy, B. Fraisse, L. Stievano, M.T. Sougrati, Alkaline-earth metal-doped perovskites $La_{0.95}A_{0.05}MnO_{3+\delta}$ (A = Ca, Sr): new structural and magnetic features revealed by ^{57}Fe Mössbauer spectroscopy and magnetic measurements, J. Phys. Chem. Solids 159 (2021) 110268, http://dx.doi.org/10.1016/j.jpcs.2021.110268.
[20] Y.-K. Liu, Y.-W. Yin, X.-G. Li, Colossal magnetoresistance in manganites and related prototype devices, Chin. Phys. B 22 (2013) 087502, http://dx.doi.org/10.1088/1674-1056/22/8/087502.
[21] D.I. Pchelina, V.D. Sedykh, N.I. Chistyakova, V.S. Rusakov, Y.A. Alekhina, A.N. Tselebrovskiy, B. Fraisse, L. Stievano, M.T. Sougrati, The structural and magnetic features of perovskite oxides $La_{1-x}Sr_xMnO_{3+\delta}$ (x = 0.05, 0.10, 0.20) depending on the strontium doping content and heat treatment, Ceram. Int. 49 (2022) 10774, http://dx.doi.org/10.1016/j.ceramint.2022.11.270.
[22] Q. Yang, G. Wang, H. Wu, B.A. Beshiwork, D. Tian, S. Zhu, Y. Yang, X. Lu, Y. Ding, Y. Ling, Y. Chen, B. Lin, A high-entropy perovskite cathode for solid oxide fuel cells, J. Alloys Compd. 872 (2021) 159633, http://dx.doi.org/10.1016/j.jallcom.2021.159633.
[23] J. Ma, Y. Pan, Y. Wang, Y. Chen, A Sr and Ni doped Ruddlesden–Popper perovskite oxide $La_{1.6}Sr_{0.4}Cu_{0.6}Ni_{0.4}O_{4+\delta}$ as a promising cathode for protonic ceramic fuel cells, J. Power Sources 509 (2021) 230369, http://dx.doi.org/10.1016/j.jpowsour.2021.230369.
[24] M. Guo, T. Xia, Q. Li, L. Sun, H. Zhao, Boosting the electrocatalytic performance of Fe-based perovskite cathode electrocatalyst for solid oxide fuel cells, J. Eur. Ceram. Soc. 41 (2021) 6531–6538, http://dx.doi.org/10.1016/j.jeurceramsoc.2021.06.054.
[25] F. Zhong, Z. Li, Y. Luo, C. Chen, C. Zhou, L. Lin, G. Cai, C. Au, L. Jiang, Geometric structure distribution and oxidation state demand of cations in spinel $Ni_xFe_{1-x}Co_2O_4$ composite cathodes for solid oxide fuel cells, Chem. Eng. J. 425 (2021) 131822, http://dx.doi.org/10.1016/j.cej.2021.131822.
[26] E.A. Agarkova, D.V. Matveev, Y.S. Fedotov, A.I. Ivanov, D.A. Agarkov, S.I. Bredikhin, Processing of manganite-based contact layers for stacking of planar solid oxide fuel cells, Mater. Lett. 309 (2022) 131462, http://dx.doi.org/10.1016/j.matlet.2021.131462.
[27] S. Durán, N. Rangel, C. Silva, M.A. Macias, E. Capoen, C. Pirovano, A. Niemczyk, L. Suescun, P. Roussel, G.H. Gauthier, Study of $La_4BaCu_{5-x}Mn_xO_{13+\delta}$ materials as potential electrode for symmetrical-SOFC, Solid State Ionics 341 (2019) 115031, http://dx.doi.org/10.1016/j.ssi.2019.115031.
[28] Y.L. Liu, K. Thydén, M. Chen, A. Hagen, Microstructure degradation of LSM–YSZ cathode in SOFCs operated at various conditions, Solid State Ionics 206 (2012) 97–103, http://dx.doi.org/10.1016/j.ssi.2011.10.020.
[29] A.A. Ostroushko, O.V. Russkikh, T.Y. Maksimchuk, Charge generation during the synthesis of doped lanthanum manganites via combustion of organo-inorganic precursors, Ceram. Int. 47 (2021) 21905–21914, http://dx.doi.org/10.1016/j.ceramint.2021.04.208.
[30] A.O. Turky, M.M. Rashad, A.M. Hassan, E.M. Elnaggar, H. Zhao, M. Bechelany, Tunable investigation optical, electrical and magnetic behaviors of Gd^{3+} substituted lanthanum strontium manganite $La_{0.5-x}Sr_{0.5}Gd_xMnO_3$ nanopowders facilely synthesized through citrate precursor technique, J. Alloys Compd. 735 (2018) 2175–2181, http://dx.doi.org/10.1016/j.jallcom.2017.11.373.
[31] R. Li, F. Jin, Y. Zhang, B. Niu, J. Liu, T. He, Performance and optimization of perovskite-type $La_{1.4}Ca_{0.6}CoMnO_{5+\delta}$ cathode for intermediate-temperature solid oxide fuel cells, Int. J. Hydrog. Energy 44 (2019) 8467–8478, http://dx.doi.org/10.1016/j.ijhydene.2019.01.296.
[32] C. Moure, O. Peña, Recent advances in perovskites: processing and properties, Prog. Solid State Chem. 43 (2015) 123–148, http://dx.doi.org/10.1016/j.progsolidstchem.2015.09.001.
[33] A.C. Ferrel-Álvarez, M.A. Domínguez-Crespo, H. Cong, A.M. Torres-Huerta, S.B. Brachetti-Sibaja, W. De La Cruz, Synthesis and surface characterization of the $La_{0.7-x}Pr_xCa_{0.3}MnO_3$ (LPCM) perovskite by a non-conventional microwave irradiation method, J. Alloys Compd. 735 (2018) 1750–1758, http://dx.doi.org/10.1016/j.jallcom.2017.11.306.
[34] A.C. Ferrel-Alvarez, M.A. Domínguez-Crespo, H. Cong, A.M. Torres-Huerta, D. Palma-Ramírez, J.T.S. Irvine, Microwave irradiation synthesis to obtain $La_{0.7-x}Pr_xCa_{0.3}MnO_3$ perovskites: electrical and electrochemical performance, J. Alloys Compd. 851 (2021) 156882, http://dx.doi.org/10.1016/j.jallcom.2020.156882.
[35] S. Lala, M. Ghosh, P.K. Das, D. Das, T. Kar, S.K. Pradhan, Magnesium substitution in carbonated hydroxyapatite: structural and microstructural characterization by Rietveld's refinement, Mater. Chem. Phys. 170 (2016) 319–329, http://dx.doi.org/10.1016/j.matchemphys.2015.12.058.
[36] E. Hernández, V. Sagredo, G.E. Delgado, Synthesis and magnetic characterization of $LaMnO_3$ nanoparticles, Rev. Mex. Fís. 61 (2015) 166–169 https://www.scielo.org.mx/scielo.php?script=sci_arttext&pid=S0035-001X2015000300003.
[37] K. Sabiruddin, J. Joardar, P.P. Bandyopadhyay, Analysis of phase transformation in plasma sprayed alumina coatings using Rietveld refinement, Surf. Coat. Technol. 204 (2010) 3248–3253, http://dx.doi.org/10.1016/j.surfcoat.2010.03.026.
[38] A. Majid, J. Tunney, S. Argue, D. Wang, M. Post, J. Margeson, Preparation of SrFeO~2.85 perovskite using a citric acid assisted Pechini-type method, J. Alloys Compd. 398 (2005) 48–54, http://dx.doi.org/10.1016/j.jallcom.2005.02.023.

[39] F. Bourguiba, A. Dhahri, T. Tahri, J. Dhahri, N. Abdelmoula, K. Taibi, E.K. Hlil, Structure properties and relax or characteristics of the phases transformation in $BaTi_{0.5}(Fe_{0.33}Mo_{0.17})O_3$ perovskite ceramic, J. Alloys Compd. 675 (2016) 174–182, http://dx.doi.org/10.1016/j.jallcom.2016.03.016.
[40] J.H. Scofield, Hartree–Slater subshell photoionization cross-sections at 1254 and 1487 eV, J. Electron Spectrosc. Relat. Phenom. 8 (1976) 129–137, http://dx.doi.org/10.1016/0368-2048(76)80015-1.
[41] N. Choudhary, M.K. Verma, N.D. Sharma, S. Sharma, D. Singh, Correlation between magnetic and transport properties of rare earth doped perovskite manganites $La_{0.6}R_{0.1}Ca_{0.3}MnO_3$ (R = La, Nd, Sm, Gd, and Dy) synthesized by Pechini process, Mater. Chem. Phys. 242 (2020) 122482, http://dx.doi.org/10.1016/j.matchemphys.2019.122482.
[42] H. Kabir, S.H. Nandyala, M.M. Rahman, M.A. Kabir, A. Stamboulis, Influence of calcination on the sol–gel synthesis of lanthanum oxide nanoparticles, Appl. Phys. A 124 (2018) 820, http://dx.doi.org/10.1007/s00339-018-2246-5.
[43] B. Mutharani, P. Ranganathan, S.-M. Chen, P. Sireesha, Ultrasound-induced radicals initiated the formation of inorganic–organic Pr_2O_3/polystyrene hybrid composite for electro-oxidative determination of chemotherapeutic drug methotrexate, Ultrason. Sonochem. 56 (2019) 410–421, http://dx.doi.org/10.1016/j.ultsonch.2019.04.029.
[44] X. Zhang, L. Liu, J. Feng, X. Ju, J. Wang, T. He, P. Chen, Ru nanoparticles on Pr_2O_3 as an efficient catalyst for hydrogen production from ammonia decomposition, Catal. Lett. 152 (2022) 1170–1181, http://dx.doi.org/10.1007/s10562-021-03709-2.
[45] M. Oumezzine, S. Hcini, M. Baazaoui, H.B. Sales, I.M.G.d. Santos, M. Oumezzine, Crystallite size effect on the structural, microstructure, magnetic and electrical transport properties of $Pr_{0.7}Sr_{0.3}Mn_{0.9}Cr_{0.1}O_3$ nanocrystalline via a modified Pechini method, J. Alloys Compd. 571 (2013) 79–84, http://dx.doi.org/10.1016/j.jallcom.2013.03.058.
[46] G.L. Luque, N.F. Ferreyra, A.G. Leyva, G.A. Rivas, Characterization of carbon paste electrodes modified with manganese based perovskites-type oxides from the amperometric determination of hydrogen peroxide, Sens. Actuators B: Chem. 142 (2009) 331–336, http://dx.doi.org/10.1016/j.snb.2009.07.038.
[47] Y. Shi, N. Ni, Q. Ding, X. Zhao, Tailoring high-temperature stability and electrical conductivity of high entropy lanthanum manganite for solid oxide fuel cell cathodes, J. Mater. Chem. A 10 (2022) 2256–2270, http://dx.doi.org/10.1039/D1TA07275G.
[48] M. Rosić, L. Kljaljević, D. Jordanov, M. Stoiljković, V. Kusigerski, V. Spasojević, B. Matović, Effects of sintering on the structural, microstructural and magnetic properties of nanoparticle manganite $Ca_{1-x}Gd_xMnO_3$ ($x = 0.05, 0.1, 0.15, 0.2$), Ceram. Int. 41 (2015) 14964–14972, http://dx.doi.org/10.1016/j.ceramint.2015.08.041.
[49] B.S. N, A. Rao, P.D. Babu, G.S. Okram, Structural, electrical, magnetic and thermal properties of $Gd_{1-x}Sr_xMnO_3$ ($0.2 \leq x \leq 0.5$) manganites, Phys. B: Condensed Matter 479 (2015) 10–20, http://dx.doi.org/10.1016/j.physb.2015.09.025.
[50] M.T. Colomer, A.L. Ortiz, V. López-Domínguez, J.M. Alonso, M.A. García, Preparation, thermal and phase evolution and functional properties of non-stoichiometric strontium-doped lanthanum manganite perovskite ceramics, J. Eur. Ceram. Soc. 37 (2017) 3527–3533, http://dx.doi.org/10.1016/j.jeurceramsoc.2017.04.019.
[51] M.T. Colomer, E. Chinarro, A.L. Ortiz, Processing and electrical conductivity of non-stoichiometric lanthanum strontium manganite perovskites prepared from powders synthesized by a polymerizable-complexation route, Ceram. Int. 44 (2018) 13389–13395, http://dx.doi.org/10.1016/j.ceramint.2018.04.175.
[52] D.I. Saparuddin, N.A.N. Hisham, S.A. Aziz, K.A. Matori, S. Honda, Y. Iwamoto, M.H.M. Zaid, Effect of sintering temperature on the crystal growth, microstructure and mechanical strength of foam glass–ceramic from waste materials, J. Mater. Res. Technol. 9 (2020) 5640–5647, http://dx.doi.org/10.1016/j.jmrt.2020.03.089.
[53] R. Venkata Krishnan, V.K. Mittal, R. Babu, A. Senapati, S. Bera, K. Nagarajan, Heat capacity measurements and XPS studies on uranium–lanthanum mixed oxides, J. Alloys Compd. 509 (2011) 3229–3237, http://dx.doi.org/10.1016/j.jallcom.2010.12.090.
[54] S.M. Kaczmarek, E. Tomaszewicz, D. Moszyński, A. Jasik, G. Leniec, DTA/TG, IR, EPR and XPS studies of some praseodymium(III) tungstates, Mater. Chem. Phys. 124 (2010) 646–651, http://dx.doi.org/10.1016/j.matchemphys.2010.07.028.
[55] A.V. Shlyakhtina, J.C.C. Abrantes, E. Gomes, A.N. Shchegolikhin, G.A. Vorobieva, K.I. Maslakov, A.V. Knotko, L.G. Shcherbakova, Effect of Pr^{3+}/Pr^{4+} ratio on the oxygen ion transport and thermomechanical properties of the pyrochlore and fluorite phases in the ZrO_2–Pr_2O_3 system, Int. J. Hydrog. Energy 41 (2016) 9982–9992, http://dx.doi.org/10.1016/j.ijhydene.2016.02.152.
[56] P.-Y. Peng, Influence of Sr substitution on catalytic performance of $LaMnO_3$/Ni metal foam composite for CO oxidation, Aerosol Air Qual. Res. 15 (2015), http://dx.doi.org/10.4209/aaqr.2014.11.0286.
[57] S. Luo, J. Li, J. Ran, R. Yangcheng, Y. Cui, Y. Zhang, J. Wang, Significant promotion of MgOy in bifunctional Pt-WOx-MgOy catalysts for the chemoselective conversion of glucose to lower polyols, Catal. Commun. 175 (2023) 106614, http://dx.doi.org/10.1016/j.catcom.2023.106614.
[58] H.A. Alcamand, H. dos Santos Oliveira, J.G. Balena, L.C. de Oliveira, P.L. Gastelois, M. Houmard, E.H.M. Nunes, Synthesis, characterization, and use of nanocast $LaMnO_3$ perovskites in the catalytic production of imine by the gas-phase oxidative coupling of benzyl alcohol to aniline, Catal. Commun. 175 (2023) 106606, http://dx.doi.org/10.1016/j.catcom.2023.106606.
[59] J. Zhao, C. Li, L. Kong, X. Wu, Y. Ma, Synthesis and characterization of calcium and manganese-doped rare earth oxide $La_{1-x}Ca_xFe_{0.9}Mn_{0.1}O_{3-\delta}$ for cathode material in IT-SOFC, J. Rare Earths 29 (2011) 1066–1069, http://dx.doi.org/10.1016/S1002-0721(10)60599-6.
[60] J.Y. Park, G.M. Choi, Electrical conductivity of Sr and Mg doped $LaAlO_3$, Solid State Ionics 154–155 (2002) 535–540, http://dx.doi.org/10.1016/S0167-2738(02)00510-6.
[61] A. Stroeva, V. Balakireva, L. Dunyushkina, V. Gorelov, Electroconductivity and nature of ion transfer in $La_{1-x}Sr_xSc_{1-y}Mg_yO_{3-\alpha}$ system ($0.01 \leq x = y \leq 0.20$) in dry and humid air, Russ. J. Electrochem. 46 (2010) 552–559, http://dx.doi.org/10.1134/S1023193510050095.